



RESEARCH PAPER

Assessing the Interrelationship of Microstructure, Properties, Drug Release Performance, and Preparation Process for Amorphous Solid Dispersions Via Noninvasive Imaging Analytics and Material Characterization

Wei Jia¹ · Phillip D. Yawman² · Keyur M. Pandya¹ · Kellie Sluga¹ · Tania Ng¹ · Dawen Kou¹ · Karthik Nagapudi¹ · Paul E. Luner^{2,3} · Aiden Zhu² · Shawn Zhang² · Hao Helen Hou¹

Received: 28 February 2022 / Accepted: 27 May 2022 / Published online: 3 June 2022
© The Author(s), under exclusive licence to Springer Science+Business Media, LLC, part of Springer Nature 2022

Abstract

Purpose The purpose of this work is to evaluate the interrelationship of microstructure, properties, and dissolution performance for amorphous solid dispersions (ASDs) prepared using different methods.

Methods ASD of GDC-0810 (50% w/w) with HPMC-AS was prepared using methods of spray drying and co-precipitation via resonant acoustic mixing. Microstructure, particulate and bulk powder properties, and dissolution performance were characterized for GDC-0810 ASDs. In addition to application of typical physical characterization tools, we have applied X-Ray Microscopy (XRM) to assess the contribution of microstructure to the characteristics of ASDs and obtain additional quantification and understanding of the drug product intermediates and tablets.

Results Both methods of spray drying and co-precipitation produced single-phase ASDs. Distinct differences in microstructure, particle size distribution, specific surface area, bulk and tapped density, were observed between GDC-0810 spray dried dispersion (SDD) and co-precipitated amorphous dispersion (cPAD) materials. The cPAD powders prepared by the resonant acoustic mixing process demonstrated superior compactibility compared to the SDD, while the compressibility of the ASDs were comparable. Both SDD powder and tablets showed higher *in vitro* dissolution than those of cPAD powders. XRM calculated total solid external surface area (S_A) normalized by calculated total solid volume (S_V) shows a strong correlation with micro dissolution data.

Conclusion Strong interrelationship of microstructure, physical properties, and dissolution performance was observed for GDC-0810 ASDs. XRM image-based analysis is a powerful tool to assess the contribution of microstructure to the characteristics of ASDs and provide mechanistic understanding of the interrelationship.

KEY WORDS amorphous solid dispersion · coprecipitation · material characterization · microstructure-property-performance-process interrelationship · spray drying

Abbreviations

| | |
|-----------|---|
| ASD | Amorphous solid dispersion |
| cPAD | Co-precipitated amorphous dispersion |
| FaSSIF-V2 | Fasted-state simulated intestinal fluid version 2 |

| | |
|-----|--------------------------|
| HME | Hot-melt extrusion |
| SD | Spray drying |
| SDD | Spray dried dispersion |
| RAM | Resonant acoustic mixing |
| VDD | Vacuum drum drying |
| XRM | X-ray microscopy |

✉ Hao Helen Hou
hou.hao@gene.com

¹ Small Molecule Pharmaceutical Sciences, Genentech Inc., 1 DNA Way, South San Francisco, California 94080, USA

² DigiM Solution LLC, 67 South Bedford Street, Suite 400 West, Burlington, Massachusetts 01803, USA

³ Triform Sciences LLC, Waterford, Connecticut 06385, USA

INTRODUCTION

In small molecule drug discovery and development portfolios, approximately 75% of compounds are poorly water-soluble and classified as Biopharmaceutical Classification

System (BCS) classes II and IV (1, 2). The pharmaceutical industry has recognized the importance of solubility and developed various strategies to either improve candidate druggability or overcome poor solubility using medicinal chemistry approaches and enabling formulation techniques (3). Formulating poorly water-soluble compounds as amorphous solid dispersions (ASDs) is one of the most promising approaches to enhance solubility and/or dissolution (4), and membrane flux (5) to improve bioavailability (6).

ASDs can be manufactured via a number of technologies which can be broadly categorized into melting/fusion-based and solvent-based methods (7). In melting/fusion-based methods, physical mixtures of drug and carrier are heated above the melting or glass transition temperature, followed by rapid cooling to solidify the drug in an amorphous state. Adequate mixing to form a homogenous molecular solution and sufficiently fast cooling are essential to the quality and performance of ASDs formed via melting/fusion techniques. Hot-melt extrusion (HME) (8, 9), especially the proprietary Meltrex™ technique, and KinetiSol® which uses a series of rapidly rotating blades that generate a large amount of energy to promote drug-carrier fusion without the need for an external heating source (10–12), are representative processes of melting/fusion-based technologies. Three-dimensional (3D) printing (13, 14), microwave-induced *in situ* amorphization (15, 16), and other melt-based methods (17, 18), have been investigated and used in ASD preparation. In solvent-based methods, drug and carrier are dissolved in a solvent system, followed by isolation of solid and solvent removal. The amount of residual solvents in the ASD must comply with regulatory guidelines since residual organic solvents carry a toxicity liability and also plasticize the ASD, which leads to the risks of phase separation and crystallization. Therefore, secondary drying is typically applied to remove the residual solvent to meet the acceptance criteria as defined in International Council for Harmonization Q3C (R8) guideline (19). Spray drying (SD) (20), electrospraying (21), fluidized bed drying (22), supercritical fluids (23), spray freeze-drying (24), and vacuum drum drying (VDD) (25), are based on the principle of solvent evaporation. Presently, HME and SD are the most commonly used technologies for commercial-scale ASD production. There is extensive literature on the advantages and limitations of these two technologies (7, 26). Despite their prevalent application in the pharmaceutical industry, researchers have consistently made efforts in exploring novel manufacturing techniques to circumvent the limitations of existing technologies.

Antisolvent co-precipitation is another solvent-based approach in producing ASDs at both small and commercial scales (6, 27). In this method, drug and polymer are dissolved in a common solvent, and then introduced into a common antisolvent to generate ASD via co-precipitation. Solid precipitates are isolated (e.g., via filtration)

followed by solvent removal and subsequent drying process. Co-precipitation is well suited for compounds with low solubility in volatile organic solvents and exhibiting high melting temperature and propensity for thermal degradation at elevated temperatures (26). It is essential that both drug and polymer are soluble in the common solvent and insoluble in the common antisolvent, and the solvent is miscible with the antisolvent. Ionic polymers which are insoluble in acidified aqueous antisolvents are primarily used for co-precipitation. Recent work has expanded the application of this technology to water-soluble nonionic polymers by using organic antisolvents (28), which makes it a promising alternative to SD and HME.

Due to the unstable nature of amorphous materials and the underlying principle for their formation, it is clear that the manufacturing technology and process conditions would impact ASD material characteristics and properties, and in turn *in vivo* performance (26, 29). Therefore, rational selection of an appropriate manufacturing technology and fundamental understanding of the impacts of process parameters on production efficiency, product quality, and performance are critical for delivering a successful ASD product. Although there are extensive studies that have investigated the choice of excipients and processes to maintain solid state stability and enhance biopharmaceutical performance, there are limited studies that assessed the effects of manufacturing technology on the microstructure and particulate properties of ASDs, and downstream processing in terms of powder flow and compaction. Davis et al. (30) studied the impacts of SD and HME on powder flow, compaction, and dissolution of an Itraconazole ASD. Spray dried powder contained fine particles and exhibited poorer powder flow, but showed better compactibility and tabletability than milled extrudates consisting of larger and denser particles. *In vitro* dissolution results revealed that higher drug release was observed from tablets containing spray dried powder than those containing milled extrudates. Schönfeld et al. (31) investigated the downstream processability of Ritonavir ASD prepared by HME, SD, and VDD. The VDD material showed acceptable powder flow and remarkable compactibility and tabletability, which makes it suitable for direct compression. In contrast, the SD material showed higher degree of elastic recovery during the decompression phase, with strong capping and lamination observed in compacts. In our previous work, we studied the impact of method of preparation (i.e., SD and co-precipitation) on the mechanical properties of an ASD (32). Co-precipitated powders prepared by either overhead mixing or resonant acoustic mixing (RAM) demonstrated superior compression behavior compared to the SD material. Because the processes of coprecipitation and SD impact the physical attributes of the resultant materials, in-depth characterization of their properties, at both the

bulk and particulate levels is necessary for understanding how they perform in downstream processing resulting in the final dosage form.

In addition to application of typical physical characterization tools, in this work we have applied X-Ray micro-computed tomography to obtain additional understanding of the drug product intermediates and tablets formed from ASDs made by different techniques. X-Ray micro-computed tomography (interchangeably termed MicroCT, XRCT or μ CT), has recently been used for microstructural assessment of tablets (33, 34), granules (35), and spray dried dispersions (36). Advances in non-invasive 3D imaging allows X-ray Microscopy (XRM) through AI-based image processing to quantitatively interrogate API or spray dried dispersion domains and morphology in powder blends and tablets (36–38).

In this study, ASD of GDC-0810 (Fig. 1) and hydroxypropyl methylcellulose acetate succinate (HPMC-AS) was chosen as the model system. GDC-0810 is a weak acid with very low intrinsic solubility (<0.06 mg/mL) (39). It is a BCS class II compound with a molecular weight of 446.9 g/mol, pKa of 4.3, log P of 6.2, and melting point of 232°C. ASD of GDC-0810 with HPMC-AS was prepared using methods of SD and co-precipitation via RAM at different accelerations. The objectives of this work were 2-fold: (1) evaluate the interrelationship of microstructure, properties, and dissolution performance for ASDs prepared using different methods and (2) apply XRM to assess the contribution of microstructure to the characteristics of ASDs.

Materials and Methods

Materials

GDC-0810 free acid was obtained from F. Hoffmann-La Roche AG, Basel, Switzerland. HPMC-AS MF grade was obtained from Shin-Etsu Chemical Co. (Tokyo, Japan). Common pharmaceutical excipients for oral solid dosage

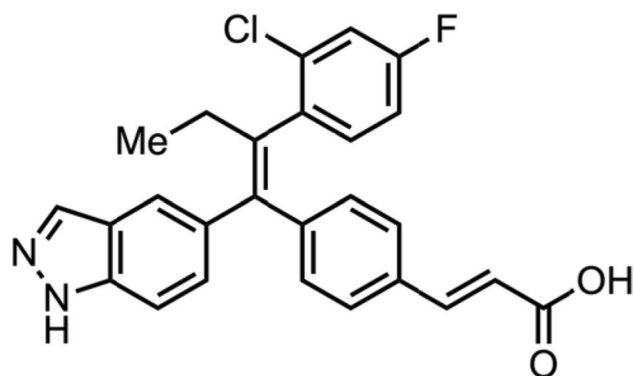


Fig. 1 Molecular structure of GDC-0810 free acid

forms were used to prepare tablets in this study: microcrystalline cellulose (Avicel PH 102, FMC Biopolymer, Philadelphia, PA, USA), lactose monohydrate (Fast Flo® 316, Foremost Farms, Rothschild, WI), croscarmellose sodium (Disolcel® GF 1506, Mingtai Chemical Co. Ltd., Bah-Der City, Taoyuan Hsien, Taiwan), colloidal silicon dioxide (Aerosil 200, Evonik Corporation, Parsippany, NJ, USA), and magnesium stearate (Ligamed MF-2-V, Peter Greven, Venlo, Netherlands).

Fasted-state simulated intestinal fluid version 2 (FaSSIF-V2) powder was purchased from Biorelevant.com (London, UK). The aqueous medium used in all experiments was 50 mM pH 6.5 sodium phosphate buffer. Buffer components and all solvents (acetonitrile, dichloromethane, and methanol) used in the study were purchased from Sigma-Aldrich Co. (St. Louis, MO).

Methods

Preparation of Amorphous Solid Dispersions (ASDs) of GDC-0810

GDC-0810 (50% w/w) ASDs were prepared by the methods of SD and co-precipitation.

- SD: GDC-0810 and HPMC-AS MF (1:1 weight ratio) were dissolved in dichloromethane/methanol (1:1 volume ratio) at a total solid load of 5% (w/v). The solution was spray-dried using a Buchi B-290 mini-spray dryer (Buchi Corp., New Castle, DE) at an inlet temperature of 85°C, outlet temperature of 45°C, and solution feed rate of 10 mL/min. A two-fluid nozzle with opening diameter of 0.5 mm was used, and the nozzle gas flow was 60 mm (measured with a Q-Flow meter from Vögtlin Instruments, Aesch, Switzerland). Secondary drying was performed at 50°C and 160 mbar for 48 hours using a vacuum oven (Thermo Fisher Scientific Lindberg/Blue M Vacuum Oven VO914).
- Co-precipitation via RAM: The RAM platform was set up as demonstrated in the previous work (32). GDC-0810 and HPMC-AS MF (1:1 weight ratio) were dissolved in DMSO at 60°C at a total solid load of 15% and the solution was then cooled to room temperature. 30 mL of the DMSO solution was introduced into a jacketed mixing vessel containing 400 mL of 0.001 N HCl maintained at 5°C using a syringe pump at a rate of 2 mL/min. The mixing was performed at an acceleration of 40 G or 80 G (where “G” is the force of gravity) for a total of 45 min. After the mixing was completed, the suspension was then filtered, and the filtrate was washed five times with 100 mL of 0.001 N HCl. The solids were dried in a vacuum oven at 50°C for 5 days. After drying, powders were milled using a

Comil (Model U5, Quadro®; Waterloo, Ontario, Canada) with a 024R screen (610 mm round hole) at the impeller speed of 1500 rpm.

Preparation of ASD Tablets

GDC-0810 ASD tablets at the dose strength of 100 mg (free acid equivalent) were prepared by a direct compression process. Table I lists the formulation composition of GDC-0810 ASD tablets in this study. Each component was manually sieved through a 30-mesh screen prior to use. Each GDC-0810 ASD powder prepared using the method mentioned above, was first blended with all excipients except for magnesium stearate on a Turbula blender (Model T2C, Glen Mills Inc., Clifton, NJ) at 67 rpm for 10 min. The mixture was then blended with magnesium stearate at the same speed for 3 min. The final blend was compressed into 15.4 mm × 7.0 mm capsule shaped tablets with a target weight of 400 ± 5 mg and a target hardness of 16 ± 2 kP using a manual press (Model C, Carver Inc., Wabash, IN).

Characterization of GDC-0810 ASDs

X-Ray Powder Diffraction (XRPD) Analysis Samples were analyzed using a Rigaku Miniflex 600 benchtop diffractometer (Rigaku Corporation, Tokyo, Japan) with Cu K α radiation (40 kV × 15 mA) in the theta/2-theta configuration (reflection mode). Samples were packed on a zero-background holder and scanned from 2 to 40° 2 θ at a scan speed of 2.0°/min and a step size of 0.020° 2 θ . Data were collected under ambient conditions and analyzed using commercial software (JADE, version 9, Materials Data Inc., Livermore, CA).

Differential Scanning Calorimetry (DSC) Modulated DSC experiments were carried out using a Q2000 differential

Table I Composition of GDC-0810 ASD Tablet, 100 mg Dose Strength

| Component | % w/w | Amount (mg/Tablet) |
|----------------------------|-------|--------------------|
| GDC-0810 ASD Powder* | 50.0 | 200 |
| Microcrystalline Cellulose | 21.5 | 86 |
| Lactose Monohydrate | 21.5 | 86 |
| Croscarmellose Sodium | 5.0 | 20 |
| Colloidal Silicon Dioxide | 1.0 | 4 |
| Magnesium Stearate | 1.0 | 4 |
| TOTAL | 100.0 | 400 |

*GDC-0810 ASD powder includes spray dried dispersion (SDD), coprecipitated amorphous dispersion (cPAD) prepared using RAM at 40G (RAM-40G) and 80G (RAM-80G), respectively

scanning calorimeter (TA Instruments, Newcastle, DE) equipped with an RCS90 refrigerated cooling system. Nitrogen gas was used as the purge gas at a flow rate of 50 mL/min. High purity indium was used to calibrate temperature and enthalpy of the instrument. Approximately 5–10 mg of ASD powder sample was packed in non-hermetically crimped pans (Tzero™ aluminum pans and pin hole lids) and heated from 5 to 200°C at 1°C/min using a temperature modulation of ±0.5°C every 60 s. Data were analyzed using commercial software (Universal Analysis 2000, TA Instruments, Newcastle, DE). The value of glass transition temperature (T_g) reported was the half height of the transition in the reversing heat flow signal.

Particle Size Distribution by Laser Diffraction The volume-based particle size distribution (PSD) of ASD powders was measured by laser diffraction using a Malvern Mastersizer 3000 equipped with the Hydro MV wet dispersion module (Malvern Instruments Inc., Westborough, MA). The dispersant used was 0.1% Span 85 in heptane (v/v). Approximately 200 mg of sample was suspended in approximately 4 mL of the dispersant. The slurry was then transferred dropwise to the Hydro MV filled with the dispersant until an obscuration of 10–20% was reached. The data were analyzed using a Mie scattering measurement principle and a general-purpose analysis model, with the refractive index of 1.39 (heptane) used for all calculations. The resulting particle size distributions were averaged from three measurements made on each material.

Brunauer–Emmett–Teller Specific Surface Area Analysis The specific surface area of ASD powders was determined by nitrogen physisorption method using a Micromeritics ASAP 2460 surface area analyzer (Micromeritics Instrument Corporation, Norcross, GA). Approximately 0.5 g of each sample was first degassed at 25°C for 72 h prior to the analysis followed by nitrogen adsorption at –196°C. Data were collected over a P/P_0 range of 0.05–0.30, and the surface area was calculated using the linear form of the Brunauer–Emmett–Teller (BET) equation.

Bulk and Tapped Density Bulk density was determined by measuring the volume of a known mass of powder in a graduated cylinder. Tapped density was determined by mechanically tapping the cylinder using a Tapped Density Tester (Series JV 2000; Copley Scientific Limited, Nottingham, UK) until there was no change in the volume. The volume of the sample was then read directly from the cylinder and used to calculate the tap density according to the relationship: mass/volume.

Powder Compression Studies Compression experiments were carried out using a servo-hydraulic compaction

simulator (HB100, Huxley Bertram Engineering Ltd., Cambridge, UK). The compaction simulator measured punch forces, displacements, and die wall pressure. Punch compliance calibration was conducted in duplicates prior to testing each material. Calibration was conducted by performing bland compression experiments (i.e., by compressing the punches against one another) using a load control profile that constantly ramped the upper punch load from 0 to 45 kN over a 10 s period and fixing the lower punch position. The punch deformation was then calculated by subtracting the lower punch position from the upper punch position as a function of load. The deformation of the punch was then added to the punch gap data collected during the instrumented die experiments. Die wall sensor calibration runs (two at each sensor: lower, middle, and upper) were also performed prior to the material compression using a 3 mm rubber slug compressed from 0 to 250 MPa.

A cylindrical 10-mm diameter instrumented die was used to measure pressure in the radial direction. Standard TSM B 10 mm flat round punches (Natoli Engineering, St Charles, MO) were used for all experiments utilizing the instrumented die. Punches and die were externally lubricated by compressing magnesium stearate into a compact prior to compressing each sample. After the magnesium stearate compact was ejected, the die was filled with approximately 350 mg of powder. The compression of each powder commenced with a gradual loading from 0.1 kN to 2 kN followed by a constant rate loading at 250 MPa/s to reach the target peak load. In this study, the peak loads varied from 3.93 kN (50 MPa) to 19.65 kN (250 MPa) at 3.93 kN (50 MPa) increments. Decompression was carried out at 2500 MPa/s until approximately 0.1 kN of load remained. The compact was held in the die for 2 s and then ejected. During the course of compression, force was applied from the upper punch and the lower punch was kept stationary. Compression was performed in duplicate at each target peak load.

Determination of Key Compaction Properties

Tensile Strength of Round Compacts At least 24 hours after compression experiments, the weight of powder compacts was determined using a balance (Model XPE205, Mettler Toledo, Zurich, Switzerland), and out-of-die dimensions were measured with a caliper (Model 537-400S, Mitutoyo, Kawasaki, Japan). Tablet breaking force values were determined using a TA.HD Plus Texture Analyzer (Stable Micro Systems, Texture Technologies, Hamilton, MA). Compacts were fractured diametrically at a testing speed of 0.35 mm/s.

Tensile strength of a round compact, σ , in MPa was calculated using Eq. (1): (22)

$$\sigma = \frac{2F}{10^6 \pi D t} \quad (1)$$

where F is the breaking force (N), D is the diameter (m), and t is the thickness (m) of a round compact.

Porosity of Round Compacts The porosity, ε , of a compact was calculated by the following equation:

$$\varepsilon = 1 - \frac{\rho}{\rho_t} \quad (2)$$

where ρ is the density which was calculated from the weight and volume of the compact. ρ_t is the true density of the powder, which was determined using a helium pycnometer (AccuPyc II 1340, Micromeritics; Norcross, GA). Approximately 0.5–2.0 g of each powder sample were filled in a 3.5-cm³ sample cup. Then true density measurement was carried out at an equilibration rate of 0.0050 psig/min and the number of purges was set to 5.

In-Die Heckel Analysis The Heckel equation (40) was derived based on the assumption that the densification of the powder bed follows the first-order kinetics. It describes the relationship between the powder bed porosity (ε) and the applied compaction pressure (P) using Eq. (3):

$$\ln \left(\frac{1}{\varepsilon} \right) = KP + A \quad (3)$$

where K is the slope of the linear region and A is the intercept. The inverse of K represents the mean yield pressure, P_y . In this work, in-die Heckel analysis was performed using compression data obtained with a maximum compaction pressure of 250 MPa to determine P_y values. In-die porosity of a compact was calculated from the minimum in-die thickness measured by the compaction simulator and tablet weight. The natural logarithm of the reciprocal of the in-die porosity was plotted as a function of the applied compaction pressure (P). Linear regression was applied to fit the linear portion of the plot to obtain the slope by progressively excluding data points until the R^2 value greater than 0.99 were obtained. Measurements were performed in duplicate.

In Vitro Dissolution Testing

Powder Dissolution Dissolution profiles of GDC-0810 ASD powders were acquired by using a μ Diss Profiler™ (Pion Inc., Billerica, MA). The dissolution medium, FaSSIF V2, degassed and preheated to 37°C prior to use. Approximately 12 mg of each ASD powder sample was added to a glass vial, followed by adding 20 mL of the medium. For each vial, the magnetic stirrer was set at 300 rpm and the temperature was maintained at 37°C. Up to eight photodiode array

(PDA) spectrophotometers were employed, each with its own dedicated fiber optic dip probe, center-positioned in the vial to monitor real time absorbance of the drug in solution. The detection wavelength selected was 365–375 nm. The path length of the UV fiber optic probes used was 10 mm. Data were collected up to 3 hr. and analyzed for real-time concentration-time profiles using AuPRO software (Pion Inc.).

Tablet Dissolution Dissolution was performed using a standard USP type II dissolution vessel (Distek Symphony 7100, North Brunswick, NJ). The medium was 500 mL of FaSSIF V2, degassed and preheated to 37°C using a Distek ezfill 4500. One tablet at dose strength of 100 mg (GDC-0810 free acid) was used in each vessel and dissolution was monitored for 75 minutes. The paddle speed was 75 rpm up to 60 minutes and was increased to 250 rpm from 60 to 75 minutes. Automated sample volumes of 1.5 mL were filtered through 10 µm polyethylene in-line filter tips (Distek, Inc., North Brunswick, NJ) at various time-points and collected in individual HPLC vials for analysis.

Sample analysis was performed using an Agilent 1200 HPLC instrument (Santa Clara, CA) controlled by Empower software (Waters Corporation, Milford, MA). Data acquisition and processing was also performed using Empower. The HPLC method used an Ascentis Express C18 column (50×3.0 mm, 2.7 µm particle size) with 0.1% formic acid in water/methanol (88:12 v/v) as mobile phase A and 0.1% formic acid in acetonitrile/methanol (88:12 v/v) as mobile phase B (MPB). A gradient program was employed, starting with a 45% MPB hold from 0 to 1.4 minutes followed by a gradient of 45% to 100% MPB in 0.8 minutes. Other HPLC parameters used were a column temperature of 40°C, flow rate of 1.2 mL/min, UV detection at 310 nm, an autosampler temperature of 5°C, and an injection volume of 6 µL. Sample quantification was performed against an external standard prepared in duplicate, with the second replicate serving as a QC control.

Focused Ion Beam-Scanning Electron Microscopy (FIB-SEM)

All sample images were acquired using a Zeiss Auriga FIB-SEM CrossBeam workstation (Carl Zeiss). SDD or cPAD powder samples were mounted on an aluminum stub with carbon tape and sputter coated with gold to reduce charging. SEM imaging was performed with electron high tension (EHT) of 2 kV, and ~5 mm working distance. A selected particle was milled with the focused ion beam at 30 kV/16 nA.

X-Ray Microscopy (XRM)

All sample images were acquired using a Zeiss Xradia Versa 520 XRM system (Carl Zeiss X-Ray Microscopy). The XRM system was equipped with a sophisticated condenser and objective lens design which allowed for the collection of high resolution images on a region of interest within the interior of the sample. SDD or cPAD powder samples were placed in plastic vials and mounted to a rotational stage between an X-Ray source and the detector. A low magnification radiograph of the entire contents of the vial was first acquired, based on which a smaller, representative region of interest (ROI) was selected for scanning at a higher resolution. Successive radiographs of this ROI were acquired through rotation of the sample over 360-degrees, using an X-ray source energy of 60 keV. About 300 radiographic projection images were reconstructed into a stack of approximately 1000 images using a filtered back projection algorithm with an effective voxel size of 1 µm. Tablet samples made from the powder sample were mounted directly to the rotational stage and imaged in the same manner.

Artificial Intelligence-Based Image Analysis

The XRM images were analyzed and quantified using DigiM I2S™ cloud-based image analysis software (DigiM Solution, LLC, MA, USA). Data from the XRM images were expressed in grayscale intensity values on a per pixel basis. Pixel grayscale intensity corresponds to density where bright grayscale contrast corresponds to high density material, darker grayscale contrast corresponds to lower density material, and black contrast corresponds to air voids or porosity. The collection of pixels from the imaging signal establishes a 3D density map of the different material components in which each material phase is characterized by a unique textural pattern. An artificial intelligence-based image segmentation (AIBIS, DigiM Solutions LLC) algorithm differentiates these unique textural patterns into various material phases. The solid phase is then further segmented into unique material components and interparticle air is separated from intraparticle air or porosity. During an AIBIS, a human analyst trains the AIBIS engine to recognize the unique textural patterns through a 10 to 15 min iterative training on a small seed image (41). The results of the training set were then applied to additional images of a sample automatically. The SDD powder sample was segmented into two material phases: non-porous solid and interparticle air. Both cPAD samples were segmented into four material phases: non-porous solid, intraparticle solid, intraparticle air (porosity), and interparticle air. Intra-particle solid and intraparticle air compose a solid particle with porosity. 3D rendering and visualization were generated using DigiM I2S™ and 3D Slicer.

The volume of a material phase was calculated as a summation of all voxels assigned to that phase (via AIBIS), multiplied by the physical dimension of a voxel. For the SDD powder sample, a solid volume fraction was calculated by the volume of non-porous solid divided by the combined volume of interparticle air and non-porous solid. For the cPAD powder samples, a total solid volume fraction was calculated by combining the non-porous solid and intra-particle solid phases. Porosity was also calculated as the volume of intraparticle air normalized by the combined volume of intraparticle air, intraparticle solid, and non-porous solid.

A number of particles reconstructed from 3D XRM were often in contact with each other due to aggregation or insufficient resolution to resolve the gap between adjacent particles. An additional marker-based watershed algorithm was used to separate particles in contact with each other. This method determined the center of each particle using a morphological erosion operation, then a distance map from the center of each particle was calculated mimicking the infill of a topological map with imaginary water. A watershed line was defined to separate two particles where the two watersheds met.

Once individual particles were identified, particle size distribution (PSD) can be calculated. The volume of each particle was converted into an equivalent spherical diameter (ESD), based on which, the entire population of particles can be represented as a PSD. Surface area was also quantified via an algorithm based on the Crofton formula. In integral geometry the Crofton formula relates the length of a curve to the expected number of times a random line intersects it. When applied to a discrete binary image this method can be used to approximate surface area by counting the intercept number of the object boundary with a set of isotropic test lines (42). Using this method, the total external surface of all solid material phases was calculated for all powder samples and then normalized by corresponding volume.

XRM Image Analysis and Image-Based Permeability Simulation for Tablets

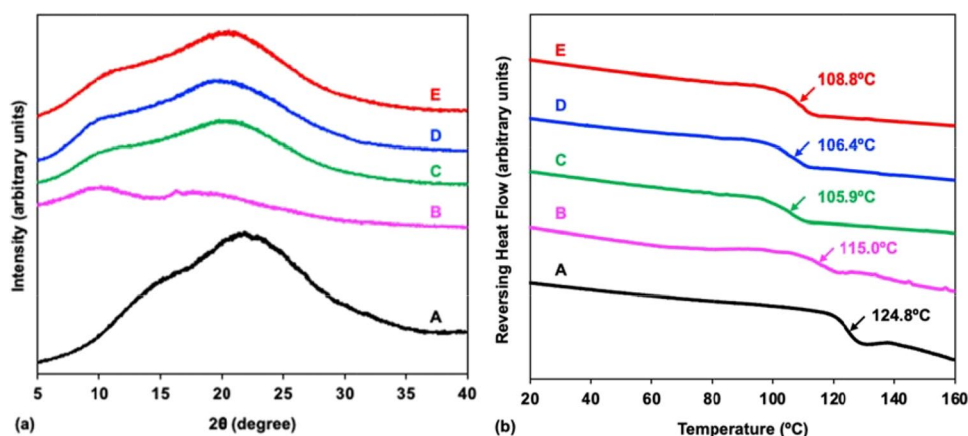
A similar AIBIS procedure was performed on the XRM data for each tablet sample to segment porosity, based on which permeability can be numerically computed. The image-based permeability simulations were conducted using DigiM I2S™. Pressure-driven fluid flow along three spatial directions were computed using a voxel-based computational fluid dynamics (CFD) solver (43). Finite volume spatial discretization was directly built on the porosity voxels of the segmented 3D image data of the tablets. The Navier-Stokes equations were then solved for flow of an incompressible fluid. After the pressure and velocity fields are solved, Darcy's law was then used to calculate permeability. This methodology has been comprehensively validated for pharmaceutical materials (44) and geoscience (45) applications.

Results

Powder Characterization of GDC-0810 ASDs

Figure 2 shows the XRPD patterns and reversing heat flow calculated from the modulated DSC thermograms for the amorphous form of GDC-0810, HPMC-AS MF polymer, and their ASDs (1:1 weight ratio) prepared by different methods, including the spray dried dispersion (SDD), and co-precipitated amorphous dispersion (cPAD) via resonant acoustic mixing (RAM) at the acceleration of 40 G (RAM-40G) and 80 G (RAM-80G). The XRPD data indicate that all the three ASD materials are amorphous. All three ASDs showed a single glass transition temperature (T_g). The T_g of the ASDs ranged from 105.9°C to 108.8°C, with SDD having slightly higher T_g than RAM-40G and RAM-80G materials. A negative deviation from ideality was observed for the T_g of ASDs, with the values lower than the T_g of the individual components (GDC-0810 ~ 125°C

Fig. 2 XRPD patterns (a) and reversing heat flow calculated from the modulated DSC thermograms (b) for (A) amorphous form of GDC-0810 (produced by spray drying), (B) HPMC-AS MF polymer (as received), (C) RAM-80G, (D) RAM-40G, (E) SDD



and HPMC-AS MF $\sim 115^\circ\text{C}$). A similar behavior has previously been reported for AMG-517/HPMC-AS ASDs (46). In a previous publication, we reported solid state NMR (SSNMR) data which indicates that the GDC-0810 ASDs prepared by spray drying and co-precipitation processes via RAM are phase mixed (32). In addition to the SSNMR data, the observation of a single T_g for all three ASDs, indicates that GDC-0810 was molecularly dispersed in HPMC-AS MF polymer in all cases.

The particle size distribution by laser diffraction, BET specific surface area, specific surface area calculated from the Sauter Mean Diameter ($D_{3,2}$), and density data for GDC-0810 ASD powders are summarized in Table II. The particle size data of the two cPAD powders, RAM-40G and RAM-80G, was fairly comparable, with the same D_{10} value. The D_{50} and D_{90} of RAM-40G powder was slightly higher than that of RAM-80G powder. The SDD powder was composed of much finer particles, with D_{50} and D_{90} of 8 and 16 μm , respectively. The D_{90} of SDD powder was even smaller than the D_{50} of both cPAD powders. In spite of the smaller particle size of the SDD, its BET specific surface area value was approximately 10-fold lower than that of the cPAD powders (RAM-40G and RAM-80G). Calculation of the specific surface area based on the $D_{3,2}$ indicates the more expected relationship where the smaller particle size material has the larger surface area. In addition, the bulk density of the two cPAD powders was approximately half of that of SDD. BET surface area, bulk

density, and SEM data indicate that the microstructure of cPAD materials is highly porous.

Compressibility and Compactibility of GDC-0810 ASDs

Compressibility is defined as the ability of a powder bed to decrease in volume under compaction pressure (47). It is one of the important properties for characterizing powder compaction behavior and is often used to quantify material plasticity. Figure 3a shows the compressibility plots (i.e., the change of out-of-die compact porosity as a function of compaction pressure) for three GDC-0810 ASDs. It appears that the compressibility plots for all three ASDs overlaid quite well, especially for RAM-40G and RAM-80G materials prepared using the co-precipitation method. The porosity of SDD compacts was only marginally higher at the same compaction pressure. The results suggest that the compressibility of GDC-0810 ASDs was not affected by their particulate properties (e.g., PSD, morphology, specific surface area) and microstructure. In addition, all three GDC-0810 ASDs demonstrated good compressibility. As the compaction pressure was lower than 150 MPa, the porosity of compacts reduced sharply with increasing the compaction pressure, from approximately 0.4 to less than 0.15. As the compaction pressure exceeded 150 MPa, the porosity further reduced, approaching to below 0.1 at the compaction pressure of 250 MPa.

Table II Summary of Physical Characterization Data for GDC-0810 ASD Powders Used in the Study. Values in parentheses indicate the standard deviations ($n=3$)

| Material | PSD by Laser Diffraction | | | | BET Specific Surface Area (m^2/g) | Specific Surface Area via $D_{3,2}$ (m^2/g) | Bulk Density (g/cm^3) | Tapped Density (g/cm^3) | True Density (g/cm^3) |
|----------|----------------------------|----------------------------|----------------------------|-----------------------------|---|---|---|---|---|
| | D_{10} (μm) | D_{50} (μm) | D_{90} (μm) | $D_{3,2}$ (μm) | | | | | |
| SDD | 1.9 (0.1) | 8.0 (0.1) | 15.3 (0.4) | 4.2 (0.1) | 2.94 (0.03) | 1.1 | 0.26 | 0.28 | 1.29 |
| RAM-40G | 5.1 (0.4) | 25.2 (0.9) | 104.0 (0.0) | 12.4 (1.3) | 34.04 (0.14) | 0.4 | 0.11 | 0.18 | 1.32 |
| RAM-80G | 4.6 (0.0) | 20.4 (0.7) | 70.0 (6.8) | 10.5 (0.3) | 31.39 (0.21) | 0.4 | 0.12 | 0.18 | 1.32 |

Fig. 3 Compressibility (a) and compactibility (b) plots of GDC-0810 ASDs (duplicate compressions at each compaction pressure). Lines on the (b) plot are the exponential fitting of the data

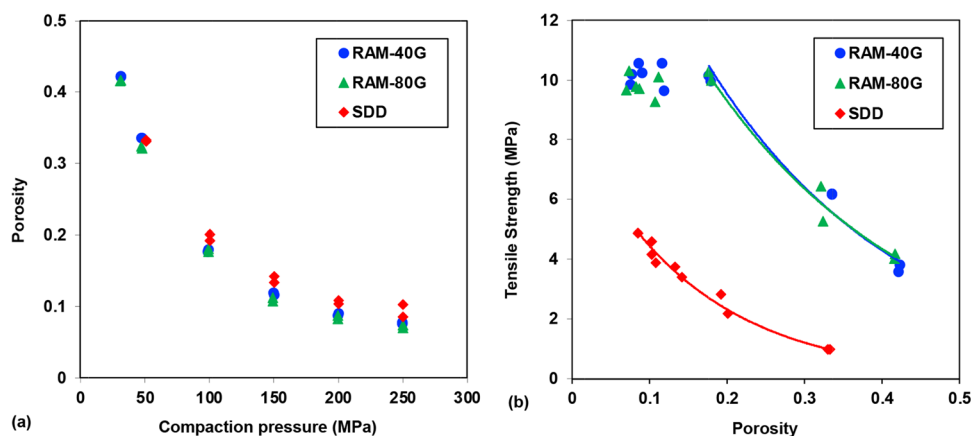


Table III Mean Yield Pressure (P_y) Obtained from In-Die Heckel Analysis for GDC-0810 ASD Powders Used in the Study. Values in parentheses indicate the standard deviations ($n=2$)

| Material | P_y (MPa) | R^2 |
|----------|-------------|--------|
| SDD | 66.4 (0.3) | 0.9999 |
| RAM-40G | 71.2 (3.2) | 0.9998 |
| RAM-80G | 70.2 (0.3) | 0.9999 |

To further quantify powder plasticity, in-die Heckel analysis (Fig. S1) was performed to obtain the mean yield pressure, P_y . The in-die P_y has been reported to be a reliable plasticity parameter (48). As listed in Table III, the average P_y values of GDC-0810 ASDs are within the range of 66–72 MPa, which are comparable to the P_y value of Avicel PH 102 (66 MPa (49)). The data suggests that GDC-0810 ASDs can be considered as ductile (plastic) materials, and show less resistance to plastic deformation during compression.

Compactibility is defined as the ability of a powdered material to be compressed into a compact of specific strength during densification (47). It is most often expressed graphically in a plot of the compact tensile strength *versus* porosity. Tablets with adequate mechanical strength are required to withstand down-stream processing and handling. As compactibility is generally independent of compaction speed, it is considered a useful tool to predict the tensile strength of tablets compressed at high speed using a rotary press during scale up (50). Figure 3b depicts the compactibility profiles for GDC-0810 ASDs. Both RAM-40G and RAM-80G materials demonstrated superior compactibility compared to SDD. As the porosity decreased from approximately 0.4 to 0.18, tensile strength of RAM-40G and RAM-80G compacts increased exponentially from approximately 4 MPa to 10 MPa. However, as the porosity further decreased, tensile strength did not change but plateaued around 10 MPa. In addition, no significant difference in compactibility between RAM-40G and RAM-80G powders was observed. Whereas, tensile strength of SDD compacts was considerably lower at a given porosity. For example, tensile strength was approximately 4 MPa at the porosity of 0.1. The strength of a compact is a reflection of interparticulate bonding that has occurred during compaction, which relates to bonding forces between individual particles, the number of bonding points, contact surface area, and bond distribution in the compact. In this work, substantially different compactibility profiles observed between RAM materials and SDD suggest that the interparticulate bonding formed in their compacts is remarkably different, with much stronger bonding formed in RAM-40G and RAM-80G compacts.

In Vitro Dissolution of GDC-0810 ASD Powders and Tablets

As described in the methods section, approximately 12 mg of each ASD sample of GDC-0810 and HPMC-AS MF

(1:1 weight ratio) was added to 20 mL of FaSSIF V2 medium for powder dissolution testing. The target GDC-0810 concentration in the medium is 300 $\mu\text{g/mL}$, which is above its crystalline solubility of 58 $\mu\text{g/mL}$ and below its amorphous solubility of 352 $\mu\text{g/mL}$ in FaSSIF V2 (see Table SI). Figure 4 shows powder dissolution profiles for three GDC-0810 ASDs. In the first 10 min, all three GDC-0810 ASD powders dissolved quickly with no difference in dissolution rate observed, reaching approximately 100 $\mu\text{g/mL}$ in the medium. Beyond this point, divergence in dissolution profiles for three materials occurred. SDD powder further dissolved, reaching ~ 200 $\mu\text{g/mL}$ at 180 min. Whereas, two cPAD powders, RAM-40G and RAM-80G, stopped further dissolving after 30 min, with GDC-0810 concentration plateaued around 115 $\mu\text{g/mL}$ until the end of the experiment. Additionally, no precipitation was observed for all three ASD powders during the testing.

In agreement with powder dissolution results, drug release from GDC-0810 SDD tablets was significantly greater than tablets prepared from RAM-40G and RAM-80G cPAD powders, as shown in Fig. 5. RAM-80G tablets showed slightly higher dissolution than RAM-40G tablets. Note that the USP2 dissolution method used in this study was under non-sink conditions, and hence, full drug release from these tablets was not obtained within 75 min. The amount of GDC-0810 dissolved from SDD tablets was approximately 50% at 75 min, whereas, it was slightly below 30% from RAM-40G and RAM-80G tablets.

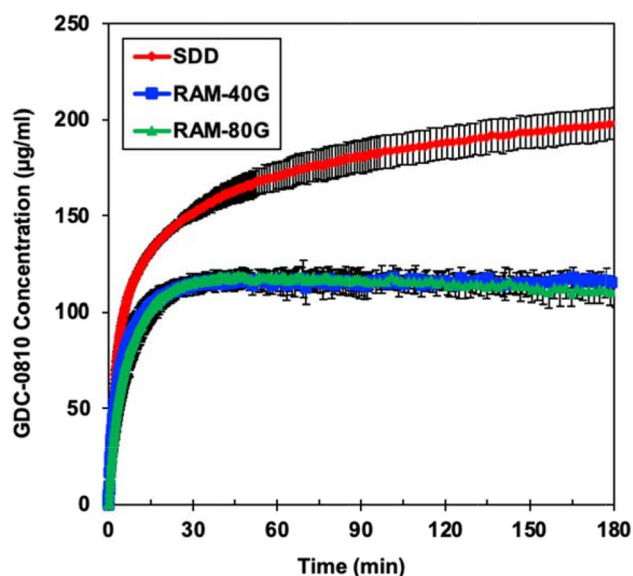


Fig. 4 Powder dissolution data for GDC-0810 ASDs. Each point represents the mean (\pm std) of three experimental values

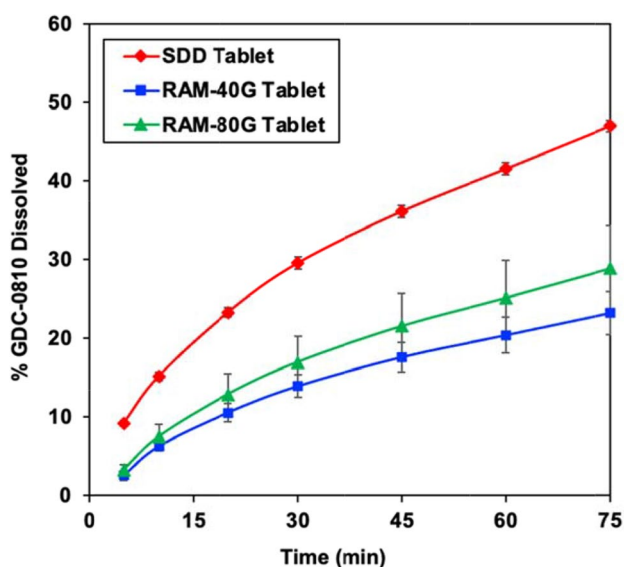


Fig. 5 USP2 dissolution data for GDC-0810 ASD tablets. Each point represents the mean (\pm std) of three experimental values

XRM Imaging Analysis

Focused Ion Beam-Scanning Electron Microscopy and X-Ray Microscopy

Surface imaging of the SDD and cPAD powder samples via scanning electron microscopy revealed the samples to have characteristic particles with distinct morphologies. The SDD material showed wrinkled dense particles with a collapsed sphere morphology (Fig. 6a1, 6b1), whereas the

cPAD material showed large irregularly shaped particles with significant surface porosity. High resolution FIB-SEM cross-section images further revealed the SDD particles to have a non-conformal geometry with no resolved porosity (Fig. 6a2), but the cPAD sample was characterized by a significant porosity network (Fig. 6b2 and 6b3) as observed by the spongy appearance in both SEM and XRM images.

While FIB-SEM enabled ultra-high resolution study of the microstructure of individual particles within the powder samples, X-ray microscopy study allowed for imaging of a much larger field of view of the powder samples. The enhanced field of view in XRM captured significantly more particles and further revealed microstructure differences between the samples. The SDD powder sampled (Fig. 6a3) showed small relatively uniformly sized primary particles with no resolved porosity. Figure 6b3 shows a RAM-40G cPAD sample at the same resolution and revealed two distinct solid material phases, dense solid particles with no resolved porosity (similar to the particles observed in the SDD sample) as well as large highly porous particles. The 2D XRM cross-sections of the tablets corresponding to SDD and cPAD powder samples (Fig. 6a4 and 6b4) also revealed microstructural differences between the tablets, most notably the SDD tablet appeared to have more abundant pores (darkest grayscale intensity phase) than the cPAD samples.

Artificial Intelligence-Based Image Analysis

As the SDD powder sample was observed to be composed of a single solid phase with no resolved porosity, the XRM dataset was segmented into two phases, solid and

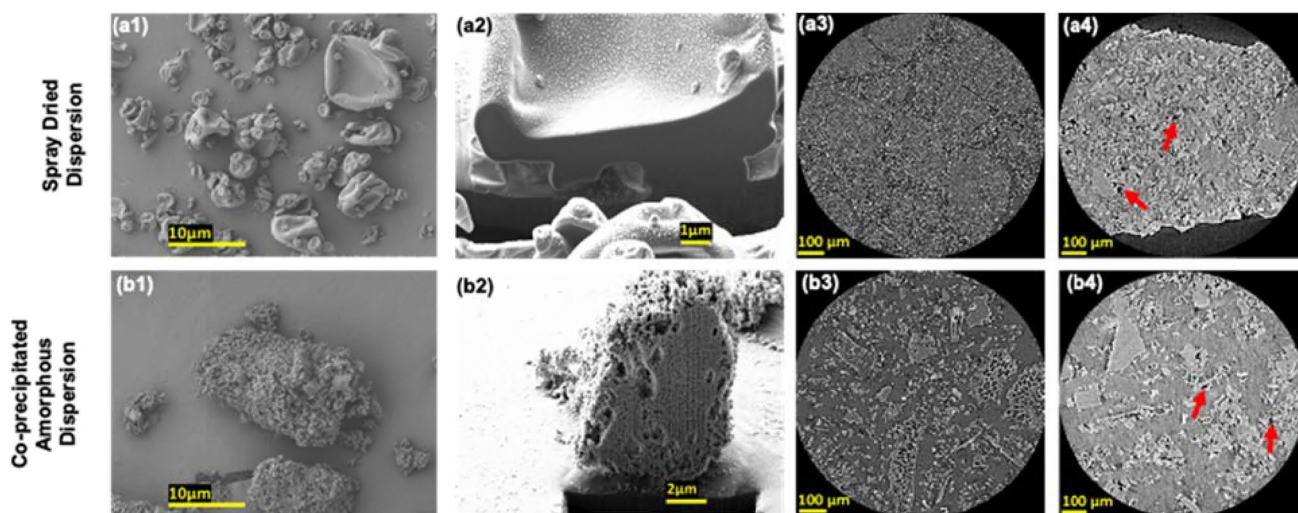


Fig. 6 Imaging modality comparison of powders and corresponding tablets: top row - spray dried dispersion (SDD), bottom row - co-precipitated amorphous dispersion (cPAD). Key: (a1) surface SEM image of SDD powder, (a2) FIB-SEM cross-section image of SDD powder, (a3) 2D cross-section image of a 3D XRM scan of SDD powder, (a4) 2D cross-section image of a 3D XRM scan of SDD tablet with example pores highlighted with red arrows. (b1) surface SEM image of RAM-40G cPAD powder, (b2) FIB-SEM cross-section image of RAM-40G cPAD powder, (b3) 2D cross-section image of a 3D XRM scan of RAM-40G cPAD powder, (b4) 2D cross-section image of a 3D XRM scan of RAM-40G cPAD tablet with example pores highlighted with red arrows

interparticle air. Figure 7a2 shows a magnified field of view from the 2D XRM cross-section of the SDD powder sample shown in Fig. 7a1. Circled in bright green is an example of a solid particle and circled in light blue is a representative region of intraparticle air. Figure 7a3 shows the final artificial intelligence–based image segmentation overlaid on the grayscale image of the magnified 2D cross-section while Figure 7a4 shows a 3D rendering of the entire SDD powder XRM volume after segmentation. Figures 7b1–7b4 represent the segmentation of a cPAD sample in the same fashion. In Fig. 7b2 an example of the dense non-porous solid in the cPAD samples are again circled in bright green and a region of interparticle air is circled in light blue. The large porous solid material unique to the cPAD samples were segmented into two additional phases, porous solid (dark green), and associated intraparticle pores (red). The segmented images from the SDD and cPAD powder samples further highlight the distinct microstructure differences between the samples.

Table IV highlights the results of quantification of pore volume, pore size distribution, and solid surface area and volume from the segmented XRM datasets. While no porosity was resolved in the SDD powder sample, the RAM-40G cPAD sample was revealed to have more than twice the porosity than that of the RAM-80G cPAD sample (10.5% and 3.9% respectively). Despite the higher pore volume in the 40G sample, both cPAD samples were found to have similar pore size distributions with comparable D_{10} , D_{50} , and D_{90} . Total solid external surface area and volume quantification again distinguished the SDD sample from the cPAD samples. When the calculated external surface area of the total solid in each sample was normalized by the respective total solid volume, the cPAD samples were found to have comparable surface area to volume ratios of $0.439 \mu\text{m}^{-1}$ for the 40G sample and $0.393 \mu\text{m}^{-1}$ for the 80G sample. The SDD powder sample on the other hand had significantly more surface area with a comparable solid volume resulting

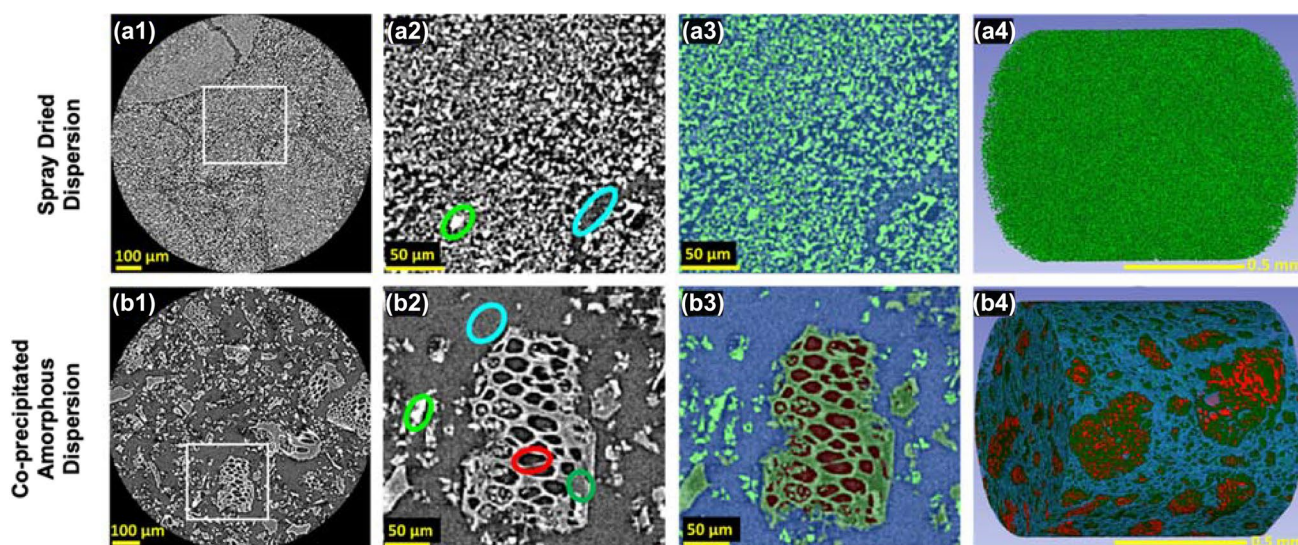


Fig. 7 Microstructure morphology and image segmentation, top row is SDD powder results and bottom row is cPAD powder results. **(a1)** 2D cross-section image of a 3D XRM scan of SDD sample. **(a2)** magnified region as highlighted in **(a1)**, interparticle air highlighted by light blue circle, solid materials highlighted by bright green circle. **(a3)** segmented interparticle air (blue), and solid material (bright green). **(a4)** 3D reconstruction of solid material in SDD powder sample. **(b1)** 2D cross-section image of a 3D XRM scan of cPAD powder sample. **(b2)** magnified region as highlighted in **(b1)** interparticle air highlighted by light blue circle, porous solid materials highlighted by dark green circles, and intraparticle pores highlighted with a red circle. **(b3)** segmented interparticle air (blue), solid material (green), and porosity (red). **(b4)** 3D reconstruction of all segmented phases in cPAD powder sample

Table IV Summary of Image-Based Characterization Data for GDC-0810 ASD Powders Used in the Study

| Material | Particle Porosity (%) | Image-Based Pore Size Distribution | | | Total Solid External Surface Area S_A (μm^2) | Total Solid Volume S_V (μm^3) | Total Solid External Surface Area/ Total Solid Volume S_A/S_V (μm^{-1}) |
|----------------|-----------------------|------------------------------------|----------------------------|----------------------------|---|--|--|
| | | D_{10} (μm) | D_{50} (μm) | D_{90} (μm) | | | |
| SDD Powder | 0 | N/A | N/A | N/A | 2.37×10^8 | 2.67×10^8 | 0.888 |
| RAM-40G Powder | 10.5 | 14 | 23 | 34 | 8.32×10^7 | 1.90×10^8 | 0.439 |
| RAM-80G Powder | 3.9 | 14 | 24 | 39 | 8.76×10^7 | 2.23×10^8 | 0.393 |

in a surface area to volume ratio nearly double that of both cPAD samples at $0.888 \mu\text{m}^{-1}$.

In comparing some of the image-based quantification data with powder dissolution data shown in Fig. 4, some interesting trends were observed. In Fig. 8, powder dissolution concentrations at 60 minutes were plotted against particle porosity as well as calculated surface area to volume ratio (S_A/S_V), respectively. As seen in Fig. 8a, powder dissolution does not correlate well with the calculated pore volume as the fastest dissolving SDD powder had no resolved porosity. In Fig. 8b on the other hand, powder dissolution data show a strong correlation with the calculated total solid external surface area (S_A) normalized by calculated total solid volume (S_V), with the amount of GDC-0810 dissolved increasing with the increase of S_A/S_V ratios.

XRM Image Analysis and Image-Based Permeability Simulation for GDC-0810 ASD Tablets

The tablet sample datasets were all segmented into two phases, solid and pore. Based on the porosity segmentation tablet pore volume and pore size distributions were calculated. As seen in Table V, the tablet samples had more comparable porosity than their associated powder with the trend in porosity reversed. The SDD tablet had the highest porosity at 17.6% followed by the RAM-80G tablet at 14.7% and the RAM-40G tablet having the lowest porosity at 12.0%. All three tablet samples were also revealed to have comparable pore size distribution. The results of the image-based

permeability simulation followed a similar trend to calculated tablet porosity where the cPAD tablets were found to have comparable permeabilities (slightly higher in the 80G sample), while the SDD tablet was found to have a permeability nearly twice that of both cPAD samples.

Tablet dissolution data were correlated with calculated tablet porosity and permeability as shown in Fig. 9 and again showed strong correlations. As seen in Fig. 9a, the percentage of GDC-0810 dissolved from ASD tablets at 60 min shows a strong correlation with calculated tablet porosity. When plotting the same tablet dissolution data points against calculated tablet permeability, the correlation is even stronger than that seen with calculated porosity (linear fitting R^2 values of 0.95 and 0.92 respectively).

Discussion

Microstructure and Particulate Properties of ASDs

Manufacturing technology and operating conditions can have a profound influence on particle microstructure and particulate properties of ASDs, such as particle size, size distribution, morphology, porosity, and surface texture/area. In general, the HME process yields a low-porosity material due to the reduction of free volume present in the polymer-drug blends during the extrusion process. Particle size and morphology of milled extrudes are typically dependent on the downstream milling process conditions. Spray-dried

Fig. 8 (a) ASD Powder dissolution (GDC-0810 concentration at 60 min) versus XRM determined particle porosity and (b) powder dissolution (GDC-0810 concentration at 60 min) versus XRM determined powder external surface area to solid volume ratio (S_A/S_V). Error bars represent standard deviations where $n=3$

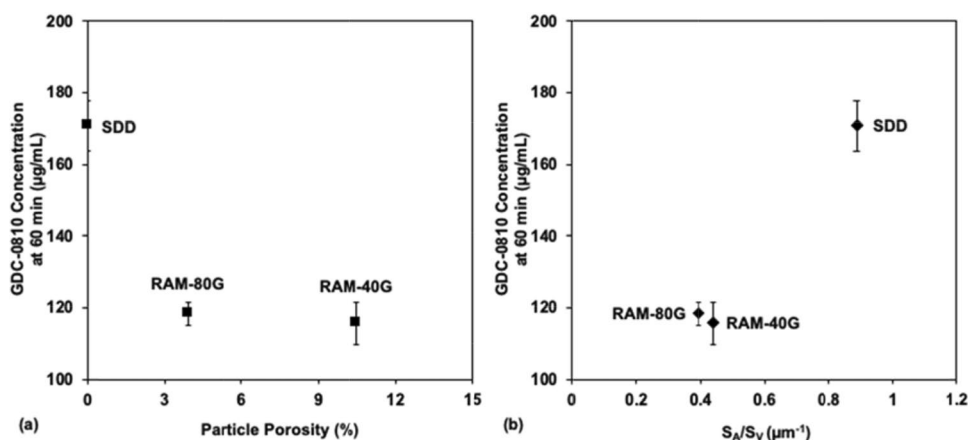
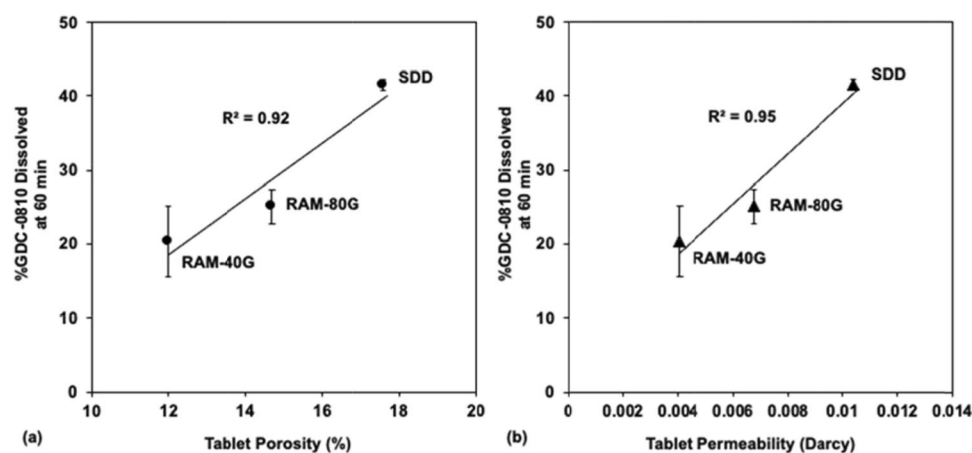


Table V Summary of Image-Based Characterization and Permeability Simulation Data for GDC-0810 ASD Tablet Used in the Study

| Material | Tablet Porosity (%) | Image-Based Pore Size Distribution | | | Permeability Kn (Darcy) |
|----------------|---------------------|------------------------------------|---------------------------------|---------------------------------|-------------------------|
| | | Pore D_{10} (μm) | Pore D_{50} (μm) | Pore D_{90} (μm) | |
| SDD Tablet | 17.6 | 11 | 18 | 23 | 0.0104 |
| RAM-40G Tablet | 12.0 | 12 | 19 | 27 | 0.0041 |
| RAM-80G Tablet | 14.7 | 12 | 19 | 27 | 0.0068 |

Fig. 9 (a) ASD tablet dissolution (%GDC-0810 dissolved at 60 min) versus XRM determined tablet porosity and (b) ASD tablet dissolution (%GDC-0810 dissolved at 60 min) versus XRM determined tablet permeability. Error bars represent standard deviations where $n=3$



particles usually have smaller particle size and exhibit an inflated or collapsed sphere shape (51). The co-precipitation process generally yields large particles with irregular shape, high porosity, and high surface area (52).

In this work, distinct differences in microstructure and particulate properties were observed between GDC-0810 SDD and cPAD materials. SDD showed wrinkled dense particles with a collapsed sphere morphology and exhibited a single solid phase with no resolved porosity. This type of morphology is based on the droplet drying mechanism of film-forming polymers. When the solvent starts to evaporate from the surface of droplets, an external solid layer (crust) is formed, reducing the diffusion of the solvent to the particle surface and thus the rate of evaporation. The inner solvent diffuses through the crust to further evaporate. Shriveled particles are formed when the partial pressure of the solvent trapped in the particle is lower (53). Previous investigation using FIB-SEM and XRM has shown that for a model system (20% MK-A and 80% HPMC-AS), SDD particle morphologies can range from hollow spheres with thin walls, to raisin-like particles with thicker shell and reduced void spaces, to solid particles with no internal voids (36). The morphology was found to be sensitive to the process conditions, in particular the outlet temperature. In the case of spray drying at small scale for the preparation of GDC-0810 SDD in this work, the process conditions resulted in the collapsed solid particle type. At the resolution of the XRM data of about 0.5 μm no porosity was observed and the particles do not have residual air pockets. In contrast, GDC-0810 cPAD materials produced in this study contained both dense non-porous solid and large irregularly shaped particles with significant surface porosity. In co-precipitation, the particle formation occurs by extraction of the solvent by the antisolvent. Generally, the solvent is highly soluble in the antisolvent, so the extraction process is very efficient resulting in amorphous particles with higher porosity compared to spray drying. Process conditions, such as precipitation rate, solvent to antisolvent ratio, temperature, and hydrodynamic

conditions, can affect the particle microstructure and properties (54). In this work, the impact of the amplitude of the mechanical vibration, referred to as the system acceleration during the RAM process, was explored. As listed in Table IV, the acceleration of 40 G resulted in co-precipitated particles with higher porosity than 80G. Despite the difference in porosity, both cPAD samples were found to have comparable pore size distributions in terms of D_{10} , D_{50} , and D_{90} . It is possible to further tailor the microstructure and particulate properties of cPAD materials by varying other conditions, e.g. precipitation rate and solvent to antisolvent ratio.

Bulk Powder Properties of ASDs

Bulk powder properties critical to downstream processing of ASDs, such as bulk and tapped densities, flow and compaction properties, can be greatly influenced by their microstructure and particulate properties. Bulk and tapped densities are measures of consolidation propensity of a powder bed under loose and tapped packing conditions respectively. GDC-0810 SDD and cPAD materials showed 2-fold difference in bulk density values due to their difference in microstructure, particle size distribution, and particle morphology. The SDD powder consisting of small wrinkled dense particles with no resolved porosity promotes denser packing and lower resistance to consolidation when compared to the cPAD powders (RAM-40G and RAM-80G) that contain large and irregularly shaped porous particles. This in turn results in the higher bulk and tapped density of the SDD powder when compared to the cPAD powders.

It has been well recognized that both intrinsic material properties (surface functional end groups, surface energy, elastic modulus, and plasticity) and particulate properties (particle size, size distribution, morphology, and surface roughness) can affect compaction properties of powders (deformation/fragmentation, tensile strength) (55). The compressibility plots (Fig. 3a) of three GDC-0810 ASD powders

overlaid fairly well, indicating that particulate properties of the three materials did not significantly impact the volume reduction of the powder bed as a result of applied pressure. In addition, comparable P_y values obtained from indie Heckel analysis for the three GDC-0810 ASD powders suggest that the three materials underwent similar deformation during the compression phase. On the other hand, as shown in the compactibility plots (Fig. 3b), RAM-40G and RAM-80G materials demonstrated superior compactibility compared to SDD. Typically, for materials undergoing plastic deformation, smaller particles result in stronger compacts than larger particles. However, an opposite trend was observed in the present work. Stronger compacts at a given solid fraction were obtained with RAM-40G and RAM-80G powders which consisted of larger particles. This observation suggests that particle size of ASD powders may not be the material attribute which caused this effect. In compaction, particles are moved into closer proximity to each other and interparticulate bonds may be established between particles. The dominating interparticle bonding mechanisms include solid bridges, mechanical interlocking, and intermolecular forces such as van der Waals forces, electrostatic force, and surface liquid capillary force (56). The predominant interparticulate bonding force between solid surfaces is the van der Waals force. Compact tensile strength is the interplay between interparticulate bonding area and bonding strength (57). Bonding strength is related to interparticulate bonding force and bonding area is dependent on intrinsic mechanical properties, particulate properties, and compaction conditions. The three GDC-0810 ASDs have the same chemical nature, and thus comparable interparticulate bonding force and bonding strength are expected. Thus, the remarkable difference in their compactibility can be ascribed to the difference in interparticulate bonding area. The large BET specific surface area, highly porous structure, and especially high surface porosity of both RAM-40G and RAM-80G powders (Fig. 6 and Table IV) led to greater bonding area between particles, and hence, stronger compacts.

Dissolution Performance of ASDs

For a given drug, dissolution performance of ASDs can be influenced by particle size, particle morphology, surface area, drug loading, polymer type, and surface energy. Particle size is important in controlling the drug release behavior. The dissolution rates of ASDs were observed to be inversely proportional to the particle size (58, 59). In general, smaller particle size corresponds to higher surface area, according to the Noyes-Whitney equation, higher surface area of the dissolving solid leads to faster dissolution rate. However, the impact of ASD particle size on its dissolution performance can be complicated when crystallization or precipitation

occurs in the dissolution media, which ultimately affects the extent and duration of supersaturation.

For GDC-0810 ASDs, both powder dissolution and tablet dissolution results revealed that SDD exhibited higher dissolution than both cPAD materials, even though the BET specific surface area of the cPAD powders (RAM-40G and RAM-80G) was approximately 10-fold higher than that of SDD, the dissolution performance does not correlate with the BET specific surface area. Similar behavior was also observed with spherical agglomerates of ferulic acid (60) and other cPAD powders (61). One hypothesis is that the internal surface area of pores present in GDC-0810 cPAD powders are not accessible to the dissolution medium due to the poor wettability, but accessible to nitrogen gas during the BET surface area measurement. Note that GDC-0810 has a log P of 6.2 and is highly hydrophobic and shows poor wettability. The surface chemical composition of particles can affect their interaction with the dissolution medium. The previous work has shown that depending on the ASD manufacturing technology, hydrophobic components can be enriched on the surface compared to the bulk and result in lower wettability of powders (62).

Additionally, the particle porosity does not correlate well with powder dissolution as the fastest dissolving SDD powder had no resolved porosity (as seen in Fig. 8b). In contrast, the calculated total solid external surface area (S_A) normalized by calculated total solid volume (S_V) obtained by XRM image analysis shows a strong correlation with powder dissolution data. These results indicate that dissolution performance of GDC-0810 ASDs is likely dictated by solid external surface area.

Application of XRM and Image-Based Analysis

In this study, three-dimensional non-invasive tomographic imaging was applied to reveal physical properties at the micro-scale that traditional characterization techniques are not able to adequately elucidate. Application of state-of-the-art artificial intelligence-based image segmentation and analysis allowed extraction of quantitative microstructure information from the XRM images that was then correlated with dissolution behavior.

While visualization of the material differences between the SDD and cPAD samples are readily observed in the FIB-SEM images, application of XRM and subsequent image-based analysis provides a quantitative and detailed perspective on how microstructure of these differently formed materials contributes to their property-performance relationships. The use of XRM to provide distinction between the external and internal features of SDD particulates and subsequent influence on performance properties has recently been reported (36, 37). In the case of the cPAD samples, the ability of the XRM analysis to obtain a normalized surface

area to integrated solid volume ratio provides a target metric for process improvement or reproducibility in contrast to a standard particle size measurement from laser diffraction which can only represent the external component of the particles.

The ability of using the XRM data to quantify both external surface area of the particles and their porosities provided a better understanding of the differences in dissolution behavior between the SDD and cPAD powder samples. Based on the experimentally obtained high BET surface area, the cPAD material would be expected to dissolve faster. However, this was not the case when the actual dissolution of the cPAD powders were measured. In addition, the XRM analysis showed that porosity of the cPAD 40G sample had more than twice the pore volume fraction relative to the 80G sample at 10.5% and 3.9%, respectively, with the SDD not having a discernible pore volume. Using the XRM data, it was possible to calculate the external particulate surface area and normalize that by the respective total solid volume (specifically with correction to not include the pore volume) and derive an external surface area to volume ratio for each powder sample. When expressed using this metric, a good correlation between external surface area to volume ratio and dissolution concentration at 60 min was observed (Fig. 8b). The S_A/S_V ratios were comparable to those calculated from the Sauter Mean Diameter ($D_{3,2}$) (c.f. Table II), a parameter that can be used for estimation of surface area.

The microstructure analysis using the XRM data also provided insight into the tablet properties both from a material property/compaction and dissolution behavior perspective. Dissolution data for each of the tablet types was consistent with their respective trends in powder dissolution. Three-dimensional non-invasive tomographic imaging provided visualization of the internal microstructure of the tablets, in particular the subsurface pore network that can influence fluid distribution and subsequent disintegration behavior. Artificial intelligence-based image segmentation of the XRM data enabled quantification of tablet porosity and pore size distribution. Although the calculated tablet pore sizes did not correlate with the dissolution results, pore volume fraction showed a strong correlation (Fig. 9a).

Liquid penetration is one of the critical parameters in the tablet dissolution process and is strongly associated with the physical properties of the tablet matrix and its interaction with fluid. Pore volume and pore size distribution only describe the amount and size of pores, not how they were interconnected or the ability of the pore network to transmit fluid. Besides the pore structure itself additional factors need to be considered when investigating liquid penetration into a porous medium. While strongly tied to the pore structure of the powder compact, tablet permeability more accurately characterizes how fluid transmits through the tablet. Advanced physical property modeling using

the quantified microstructure results was implemented to numerically compute the permeability of each tablet based on the segmented pore network in 3D. When permeability was correlated with tablet dissolution at 60 min, an improved correlation was observed ($R^2 = 0.95$) when compared to the correlation between dissolution and pore size ($R^2 = 0.92$). The permeability impact on disintegration and subsequent dissolution are convoluted by many parameters from formulation, processing, and release kinetics. While study of additional tablets would be required to more accurately correlate permeability with tablet dissolution or disintegration, the strong correlation observed here and in the literature between tablet permeability and tablet dissolution further reinforce the critically fundamental role of tablet microstructure in the many aspects of dissolution (63).

The various approaches accessible using the XRM derived data to selectively separate components, pore vs. solid regions and obtain quantitative internal and external morphological descriptions of dosage form components is expected to find increased utility in characterizing pharmaceutical systems. The application of AI to the 3D grey scale images additionally allows for understanding of not only the API component but also of the excipients and the intermediate powder or granule or the finished dosage form. Furthermore, the ability to then use the image based microstructural data to “measure” porosity and permeability (38) and also conduct mechanistically based performance simulations (64) can reduce the need for time-consuming specialized ancillary testing.

Conclusion

A systematic implementation of materials science tetrahedron (MST) principle which depicts the interrelationship among structure, property, performance and processing (65) has been broadly recognized as an indispensable tool in advancing pharmaceutical research and product development. To study such interrelationship for ASDs, GDC-0810 (50% w/w) with HPMC-AS ASDs were prepared using methods of spray drying and co-precipitation via resonant acoustic mixing at different accelerations. The application of XRM image-based analysis provides a unique ability to assess the contribution of microstructure to the characteristics of ASDs and gain clearer mechanistic understanding of the interrelationship among properties and performance. GDC-0810 cPAD powders containing coarser particles demonstrated superior compactability compared to the fine SDD powder. This was attributed to their highly porous microstructure which promoted interparticulate bonding area leading to stronger compacts. On the other hand, the SDD powder showed greater extent of dissolution than both cPAD materials. It was found that powder dissolution performance

did not correlate with the BET specific surface area or the particle porosity. Instead, a strong correlation between the external surface area to volume ratio obtained from XRM image analysis and dissolution was observed. Deeper understanding of the interrelationship of structure-properties-performance-process will provide insights when designing ASD formulations, and guide the selection of manufacturing technology and the process optimization to deliver ASDs with desired properties and performance. Downstream development of the final dosage form of ASDs could be greatly dependent on the material attributes of ASDs, especially when high ASD loading in the final drug product is needed to achieve the target dose without potential pill burden. Therefore, improving ASD properties to meet the requirements for high-quality ASD drug products is one of the key elements at the development stage. The interrelationship of structure-properties-performance-process is the foundation of a holistic approach for integrated drug development and reflects a collaborative effort across multiple functions within the technical development team throughout the entire development cycle of a drug.

Supplementary Information The online version contains supplementary material available at <https://doi.org/10.1007/s11095-022-03308-9>.

ACKNOWLEDGMENTS AND DISCLOSURES The authors declare that they have no known competing financial interests or personal relationships that could have appeared to influence the work reported in this paper.

Funding This study was internally funded by Genentech Inc.

References

- Di L, Kerns EH, Carter GT. Drug-like property concepts in pharmaceutical design. *Curr Pharm Des.* 2009;15(19):2184–94.
- Benet LZ, Broccatelli F, Oprea TI. BDDCS applied to over 900 drugs. *AAPS J.* 2011;13(4):519–47.
- Di L, Fish PV, Mano T. Bridging solubility between drug discovery and development. *Drug Discov Today.* 2012;17(9–10):486–95.
- Vaka SR, Bommana MM, Desai D, Djordjevic J, Phuapradit W, Shah N. Excipients for amorphous solid dispersions. In *amorphous solid dispersions 2014*. p. 123–161. Springer, New York, NY.
- Miller JM, Beig A, Carr RA, Spence JK, Dahan A. A win–win solution in oral delivery of lipophilic drugs: supersaturation via amorphous solid dispersions increases apparent solubility without sacrifice of intestinal membrane permeability. *Mol Pharm.* 2012;9(7):2009–16.
- Shah N, Iyer RM, Mair HJ, Choi D, Tian H, Diodone R, Fahrnich K, Pabst-Ravot A, Tang K, Scheubel E, Grippo JF. Improved human bioavailability of vemurafenib, a practically insoluble drug, using an amorphous polymer-stabilized solid dispersion prepared by a solvent-controlled coprecipitation process. *J Pharm Sci.* 2013;102(3):967–81.
- Bhujbal SV, Mitra B, Jain U, Gong Y, Agrawal A, Karki S, Taylor LS, Kumar S, Zhou QT. Pharmaceutical amorphous solid dispersion: a review of manufacturing strategies. *Acta Pharm Sin B.* 2021;11(8):2505–36.
- Repka MA, Shah S, Lu J, Maddineni S, Morott J, Patwardhan K, Mohammed NN. Melt extrusion: process to product. *Expert Opin Drug Discov.* 2012;9(1):105–25.
- Patil H, Tiwari RV, Repka MA. Hot-melt extrusion: from theory to application in pharmaceutical formulation. *AAPS PharmSciTech.* 2016;17(1):20–42.
- DiNunzio JC, Brough C, Miller DA, Williams RO III, McGinity JW. Applications of KinetiSol® dispersing for the production of plasticizer free amorphous solid dispersions. *Eur J Pharm Sci.* 2010;40(3):179–87.
- DiNunzio JC, Brough C, Miller DA, Williams RO III, McGinity JW. Fusion processing of itraconazole solid dispersions by KinetiSol® dispersing: a comparative study to hot melt extrusion. *J Pharm Sci.* 2010;99(3):1239–53.
- Ellenberger DJ, Miller DA, Williams RO. Expanding the application and formulation space of amorphous solid dispersions with KinetiSol®: a review. *AAPS PharmSciTech.* 2018;19(5):1933–56.
- Alhijaj M, Belton P, Qi S. An investigation into the use of polymer blends to improve the printability of and regulate drug release from pharmaceutical solid dispersions prepared via fused deposition modeling (FDM) 3D printing. *Eur J Pharm Biopharm.* 2016;108:111–25.
- Tan DK, Maniruzzaman M, Nokhodchi A. Advanced pharmaceutical applications of hot-melt extrusion coupled with fused deposition modeling (FDM) 3D printing for personalised drug delivery. *Pharmaceutics.* 2018;10(4):203.
- Moneghini M, Bellich B, Baxa P, Princivalle F. Microwave generated solid dispersions containing ibuprofen. *Int J Pharm.* 2008;361(1–2):125–30.
- Doreth M, Hussein MA, Priemel PA, Grohgan H, Holm R, de Diego HL, Rades T, Löbmann K. Amorphization within the tablet: using microwave irradiation to form a glass solution in situ. *Int J Pharm.* 2017;519(1–2):343–51.
- Fini A, Fernández-Hervás MJ, Holgado MA, Rodríguez L, Cavallari C, Passerini N, Caputo O. Fractal analysis of β -cyclodextrin-indomethacin particles compacted by ultrasound. *J Pharm Sci.* 1997;86(11):1303–9.
- Guo Z, Boyce C, Rhodes T, Liu L, Salituro GM, Lee KJ, Bak A, Leung DH. A novel method for preparing stabilized amorphous solid dispersion drug formulations using acoustic fusion. *Int J Pharm.* 2021;592:120026.
- International Council for Harmonisation FDA 2021. Q3C(R8) Impurities: Guidance for Residual Solvents.
- Singh A, Van den Mooter G. Spray drying formulation of amorphous solid dispersions. *Adv Drug Deliv Rev.* 2016;100:27–50.
- Nguyen DN, Clasen C, Van den Mooter G. Pharmaceutical applications of electrospraying. *J Pharm Sci.* 2016;105(9):2601–20.
- Kwon HJ, Heo EJ, Kim YH, Kim S, Hwang YH, Byun JM, Cheon SH, Park SY, Kim DY, Cho KH, Maeng HJ. Development and evaluation of poorly water-soluble celecoxib as solid dispersions containing nonionic surfactants using fluidized-bed granulation. *Pharmaceutics.* 2019;11(3):136.
- Pasquali I, Bettini R, Giordano F. Supercritical fluid technologies: an innovative approach for manipulating the solid-state of pharmaceuticals. *Adv Drug Deliv Rev.* 2008;60(3):399–410.
- Wang ZL, Finlay WH, Pepler MS, Sweeney LG. Powder formation by atmospheric spray-freeze-drying. *Powder Technol.* 2006;170(1):45–52.
- Schönfeld B, Westedt U, Wagner KG. Vacuum drum drying—a novel solvent-evaporation based technology to manufacture amorphous solid dispersions in comparison to spray drying and hot melt extrusion. *Int J Pharm.* 2021;596:120233.
- Huang S, Williams RO. Effects of the preparation process on the properties of amorphous solid dispersions. *AAPS PharmSciTech.* 2018;19(5):1971–84.

27. Song S, Wang C, Wang S, Siegel RA, Sun CC. Efficient development of sorafenib tablets with improved oral bioavailability enabled by coprecipitated amorphous solid dispersion. *Int J Pharm.* 2021;610:121216.
28. Mann AK, Schenck L, Koynov A, Rumondor AC, Jin X, Marota M, Dalton C. Producing amorphous solid dispersions via coprecipitation and spray drying: impact to physicochemical and biopharmaceutical properties. *J Pharm Sci.* 2018;107(1):183–91.
29. Vasconcelos T, Marques S, das Neves J, Sarmento B. Amorphous solid dispersions: rational selection of a manufacturing process. *Adv Drug Deliv Rev.* 2016;100:85–101.
30. Davis MT, Potter CB, Walker GM. Downstream processing of a ternary amorphous solid dispersion: the impacts of spray drying and hot melt extrusion on powder flow, compression and dissolution. *Int J Pharm.* 2018;544(1):242–53.
31. Schönfeld BV, Westedt U, Wagner KG. Compression of amorphous solid dispersions prepared by hot-melt extrusion, spray drying and vacuum drum drying. *Int J Pharm: X.* 2021;3:100102.
32. Hou HH, Rajesh A, Pandya KM, Lubach JW, Muliadi A, Yost E, Jia W, Nagapudi K. Impact of method of preparation of amorphous solid dispersions on mechanical properties: comparison of coprecipitation and spray drying. *J Pharm Sci.* 2019;108(2):870–9.
33. Schomberg AK, Diener A, Wunsch I, Finke JH, Kwade A. The use of X-ray microtomography to investigate the microstructure of pharmaceutical tablets: potentials and comparison to common physical methods. *Int J Pharm.* 2021;3:100090.
34. Yost E, Chalus P, Zhang S, Peter S, Narang AS. Quantitative X-ray microcomputed tomography assessment of internal tablet defects. *J Pharm Sci.* 2019;108(5):1818–30. <https://doi.org/10.1016/j.xphs.2018.12.024>.
35. Zhu *et al.* Investigation of quantitative X-ray microscopy for assessment of API and excipient microstructure evolution in solid dosage processing. *AAPS PharmSciTech.* In review, 2022.
36. Xi H, Zhu A, Klinzing GR, Zhou L, Zhang S, Gmitter AJ, *et al.* Characterization of spray dried particles through microstructural imaging. *J Pharm Sci.* 2020;109(11):3404–12. <https://doi.org/10.1016/j.xphs.2020.07.032>.
37. Gamble JF, Tobyn M, Zhang S, Zhu A, Salplachta J, Matula J, *et al.* Characterization of the morphological nature of hollow spray dried dispersion particles using X-ray submicron-computed tomography. *AAPS PharmSciTech.* 2021;23(1):40. <https://doi.org/10.1208/s12249-021-02184-7>.
38. Zhang S, Stroud PA, Zhu A, Johnson MJ, Lomeo J, Burcham CL, *et al.* Characterizing the impact of spray dried particle morphology on tablet dissolution using quantitative X-ray microscopy. *Eur J Pharm Sci.* 2021;165:105921. <https://doi.org/10.1016/j.ejps.2021.105921>.
39. Hou HH, Jia W, Liu L, Cheeti S, Li J, Nauka E, Nagapudi K. Effect of microenvironmental pH modulation on the dissolution rate and oral absorption of the salt of a weak acid—case study of GDC-0810. *Pharm Res.* 2018;35(2):1–11.
40. Heckel RW. Density–pressure relationships in powder compaction. *Trans Metall Soc AIME.* 1961;221(4):671–5.
41. Zhang S, Byrnes AP, Jankovic J, Neilly J. Management, analysis, and simulation of micrographs with cloud computing. *Microscopy Today.* 2019;27(2):26–33.
42. Lehmann G, Legland D. Efficient N-dimensional surface estimation using Crofton formula and run-length encoding. *The Insight Journal.* 2012.
43. Zhang S, Byrne G. Characterization of transport mechanisms for controlled release polymer membranes using focused ion beam scanning electron microscopy image-based modeling. *J Drug Deliv Sci Technol.* 2021;61:102136.
44. Jankovic J, Zhang S, Putz A, Saha MS, Susac D. Multiscale imaging and transport modeling for fuel cell electrodes. *J Mater Res.* 2019;34(4):579–91.
45. Byrnes AP, Zhang S, Canter L, Sonnenfeld MD. Application of integrated core and 3D image rock physics to characterize Niobara chalk properties including relative permeability with bound water effect. In *Unconventional Resources Technology Conference*, 2017, Austin, Texas.
46. Calahan JL, Azali SC, Munson EJ, Nagapudi K. Investigation of phase mixing in amorphous solid dispersions of AMG 517 in HPMC-AS using DSC, solid-state NMR, and solution calorimetry. *Mol Pharm.* 2015;12(11):4115–23.
47. Leuenberger H. The compressibility and compactibility of powder systems. *Int J Pharm.* 1982;12(1):41–55.
48. Vreeman G, Sun CC. Mean yield pressure from the in-die Heckel analysis is a reliable plasticity parameter. *Int J Pharm.* 2021;3:100094.
49. Yost E, Mazel V, Sluga K, Nagapudi K, Muliadi AR. Beyond Brittle/Ductile Classification: Applying Proper Constitutive Mechanical Metrics to Understand the Compression Characteristics of Pharmaceutical Materials. *J Pharm Sci.* 2022. In Press. <https://doi.org/10.1016/j.xphs.2022.01.004>.
50. Tye CK, Sun CC, Amidon GE. Evaluation of the effects of tableting speed on the relationships between compaction pressure, tablet tensile strength, and tablet solid fraction. *J Pharm Sci.* 2005;94(3):465–72.
51. Nandiyanto AB, Okuyama K. Progress in developing spray-drying methods for the production of controlled morphology particles: from the nanometer to submicrometer size ranges. *Advanced Powder Technol.* 2011;22(1):1–9.
52. Schenck L, Boyce C, Frank D, Koranne S, Ferguson HM, Strotman N. Hierarchical particle approach for co-precipitated amorphous solid dispersions for use in preclinical in vivo studies. *Pharmaceutics.* 2021;13(7):1034.
53. Esposito E, Roncarati R, Cortesi R, Cervellati F, Nastruzzi C. Production of Eudragit microparticles by spray-drying technique: influence of experimental parameters on morphological and dimensional characteristics. *Pharm Dev Technol.* 2000;5(2):267–78.
54. Shah N, Sandhu H, Phuapradit W, Pinal R, Iyer R, Albano A, Chatterji A, Anand S, Choi DS, Tang K, Tian H. Development of novel microprecipitated bulk powder (MBP) technology for manufacturing stable amorphous formulations of poorly soluble drugs. *Int J Pharm.* 2012;438(1–2):53–60.
55. Shah UV, Karde V, Ghoroi C, Heng JY. Influence of particle properties on powder bulk behaviour and processability. *Int J Pharm.* 2017;518(1–2):138–54.
56. Li Q, Rudolph V, Weigl B, Earl A. Interparticle van der Waals force in powder flowability and compactibility. *Int J Pharm.* 2004;280(1–2):77–93.
57. Sun CC. Decoding powder tableability: roles of particle adhesion and plasticity. *J Adhes Sci Technol.* 2011;25(4–5):483–99.
58. Zheng K, Lin Z, Capece M, Kunnath K, Chen L, Davé RN. Effect of particle size and polymer loading on dissolution behavior of amorphous griseofulvin powder. *J Pharm Sci.* 2019;108(1):234–42.
59. Monschke M, Kayser K, Wagner KG. Influence of particle size and drug load on amorphous solid dispersions containing pH-dependent soluble polymers and the weak base ketoconazole. *AAPS PharmSciTech.* 2021;22(1):1–1.
60. Chen H, Wang C, Kang H, Zhi B, Haynes CL, Aburub A, Sun CC. Microstructures and pharmaceutical properties of ferulic acid agglomerates prepared by different spherical crystallization methods. *Int J Pharm.* 2020;574:118914.
61. Schenck L, Mann AK, Liu Z, Milewski M, Zhang S, Ren J, Dewitt K, Hermans A, Cote A. Building a better particle: leveraging physicochemical understanding of amorphous solid dispersions and a hierarchical particle approach for improved delivery at high drug loadings. *Int J Pharm.* 2019;559:147–55.

62. Dahlberg C, Millqvist-Fureby A, Schuleit M. Surface composition and contact angle relationships for differently prepared solid dispersions. *Eur J Pharm Biopharm.* 2008;70(2):478–85.
63. Zhang S, Byrne G. Characterization of transport mechanisms for controlled release polymer membranes using focused ion beam scanning electron microscopy image-based modelling. *J Drug Deliv Sci Technol.* 2021;61:102136.
64. Zhang S, Wu D, Zhou L. Characterization of controlled release microspheres using FIB-SEM and image-based release prediction. *AAPS PharmSciTech.* 2020;21(5):194. <https://doi.org/10.1208/s12249-020-01741-w>.
65. Sun CC. Materials science tetrahedron-a useful tool for pharmaceutical research and development. *J Pharm Sci.* 2009;98(5):1671–87.

Publisher's Note Springer Nature remains neutral with regard to jurisdictional claims in published maps and institutional affiliations.